Acta Oceanol. Sin., 2017, Vol. 36, No. 8, P. 66–75
DOI: 10.1007/s13131-017-1020-4
http://www.hyxb.org.cn
E-mail: hyxbe@263.net

Observed and modelled snow and ice thickness in the Arctic Ocean with CHINARE buoy data

TIAN Zhongxiang[1, 3], CHENG Bin[2, 5*], ZHAO Jiechen[3], VIHMA Timo[2], ZHANG Wenliang[4], LI Zhijun[5], ZHANG Zhanhai[6]

[1] Ocean University of China (OUC), Qingdao 266100, China

[2] Finnish Meteorological Institute (FMI), Helsinki FI 00931, Finland

[3] National Marine Environmental Forecasting Centre (NMEFC), Beijing 100081, China

[4] National Ocean Technology Center (NOTC), Tianjin 300112, China

[5] Dalian University of Technology (DUT), Dalian 116024, China

[6] Key Laboratory for Polar Science of the State Oceanic Administration, Polar Research Institute of China, Shanghai 200136, China

Received 2 March 2016; accepted 5 July 2016

Abstract

Sea ice and the snow pack on top of it were investigated using Chinese National Arctic Research Expedition (CHINARE) buoy data. Two polar hydrometeorological drifters, known as Zeno® ice stations, were deployed during CHINARE 2003. A new type of high-resolution Snow and Ice Mass Balance Arrays, known as SIMBA buoys, were deployed during CHINARE 2014. Data from those buoys were applied to investigate the thickness of sea ice and snow in the CHINARE domain. A simple approach was applied to estimate the average snow thickness on the basis of Zeno® temperature data. Snow and ice thicknesses were also derived from vertical temperature profile data based on the SIMBA buoys. A one-dimensional snow and ice thermodynamic model (HIGHTSI) was applied to calculate the snow and ice thickness along the buoy drift trajectories. The model forcing was based on forecasts and analyses of the European Centre for Medium-Range Weather Forecasts (ECMWF). The Zeno® buoys drifted in a confined area during 2003–2004. The snow thickness modelled applying HIGHTSI was consistent with results based on Zeno® buoy data. The SIMBA buoys drifted from 81.1°N, 157.4°W to 73.5°N, 134.9°W in 15 months during 2014–2015. The total ice thickness increased from an initial August 2014 value of 1.97 m to a maximum value of 2.45 m before the onset of snow melt in May 2015; the last observation was approximately 1 m in late November 2015. The ice thickness based on HIGHTSI agreed with SIMBA measurements, in particular when the seasonal variation of oceanic heat flux was taken into account, but the modelled snow thickness differed from the observed one. Sea ice thickness derived from SIMBA data was reasonably good in cold conditions, but challenges remain in both snow and ice thickness in summer.

Key words: temperature, snow, sea ice, thickness, ice mass balance buoy, Arctic Ocean

Citation: Tian Zhongxiang, Cheng Bin, Zhao Jiechen, Vihma Timo, Zhang Wenliang, Li Zhijun, Zhang Zhanhai. 2017. Observed and modelled snow and ice thickness in the Arctic Ocean with CHINARE buoy data. Acta Oceanologica Sinica, 36(8): 66–75, doi: 10.1007/s13131-017-1020-4

1 Introduction

Sea ice is a critical component of the Arctic system, playing an important role also in the global climate system. Sea ice is sensitive to atmospheric and oceanic variability, because many climate feedbacks are linked with or enhanced by sea ice. The average sea ice thickness in the Arctic Ocean has been considerably reduced in the past 30 years. The air temperature increase over the Arctic Ocean has been at least twice as fast as the global average (Blunden and Arndt, 2012). The most dramatic indicators of the Arctic warming are the decreases of sea ice extent, concentration, thickness, as well as the duration of the ice season (e.g., Cavalieri and Parkinson, 2012).

Remote sensing methods have been extensively used to monitor sea ice extent and thickness in the Arctic Ocean (Kwok and Rothrock, 2009). The most accurate sea ice thickness information, however, still comes from *in situ* measurements. Long-term ice gauge measurements have been carried out during year-round field expeditions in the Arctic Ocean, such as the ice camps of SHEBA (Uttal et al., 2002) and DAMOCLES/Tara (Gascard et al., 2008). In addition, there has been a number of short term ice expeditions, such as the Chinese National Arctic Research Expedition (CHINARE) program (e.g., Zhang, 2004), where sparse borehole measurements on ice thickness were taken during 2–4 months over a broad region. The CHINARE program started in 1999. The Chinese ice breaker R/V *Xuelong* has been used as a platform to carry out comprehensive field expedi-

Foundation item: The National Natural Science Foundation of China under contract Nos 41428603, 41376188, 41376005 and 41506221; the Academy of Finland under contract No. 283101; the Chinese Arctic and Antarctic Administration Project under contract No. 201614; the Chinese Polar Environment Comprehensive Investigation and Assessment Programs under contract No. CHINARE-03-01.

*Corresponding author, E-mail: bin.cheng@fmi.fi

tions mainly in the Chukchi Sea and Beaufort Sea (Fig. 1). The voyages have been carried out every four to five years during Arctic summer-fall seasons. Since 2008, a field expedition has been made every second year.

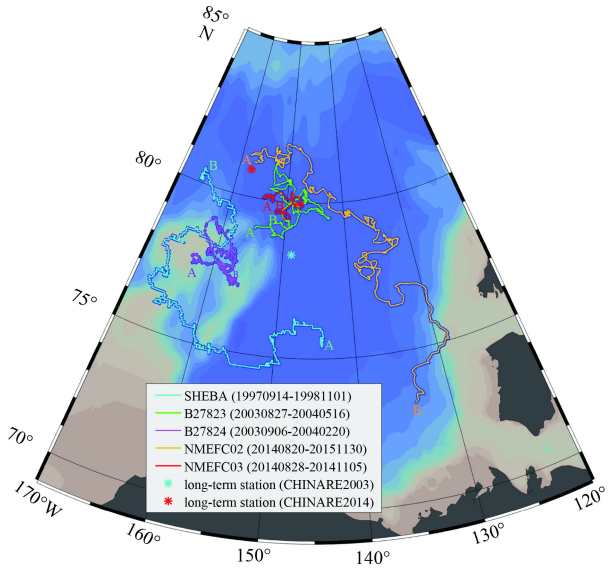

Fig. 1. Map of the CHINARE Arctic expedition domain with the drift trajectories of Zeno® and SIMBA buoys deployed during CHINARE 2003 and 2014 programs. A and B represent the buoy initial and last recorded positions, respectively. The initial long-term ice camps of CHINARE 2003 and 2014 are marked with * symbols. The SHEBA ice camp (light blue) drift trajectory is also shown.

In order to obtain long-term data on sea ice thickness, sea ice mass balance buoys (IMB) have been used. The classical IMB was developed by the U. S. Cold Regions Research and Engineering Laboratory (CRREL) jointly with MetOcean Ltd. The CRREL IMB is equipped with sophisticated acoustic sounders to measure the positions of the snow surface and ice bottom, which allows determining the thickness of snow and ice (Richter-Menge et al., 2006). This type of ice mass balance buoys have been widely used to monitor snow and ice thickness in the Arctic Ocean (e.g., Perovich et al., 2003; Lei et al., 2014). In addition, Zeno® ice station buoy developed by Coastal Environmental Systems Inc. was used during the CHINARE expedition of 2003–2004. In recent years, a novel and innovative ice mass balance buoy, known as a high-resolution sea ice mass balance array (SIMBA), was developed by the Scottish Association for Marine Sciences (SAMS). It is a new type of IMB targeted for snow and ice mass balance measurement (Jackson et al., 2013). The cost-cutting design of SIMBA makes it applicable for snow and ice monitoring and ice thickness and energy balance studies in seasonally ice-covered seas and lakes (Cheng et al., 2014). However, not many results have been published based on SIMBA application in the Arctic Ocean.

In this study, we present snow and ice thickness analyses from CHINARE buoy data. The Zeno® ice buoy was used during CHINARE 2003, yielding data on air, snow, and ice temperatures. We demonstrate a simple method to analyse snow thickness on the basis of ice temperature measurements in cold conditions. The SIMBA buoys were deployed during CHINARE 2014. The high resolution vertical temperature profiles from the ocean through ice and snow to atmosphere are used to derive snow and ice thickness. A high-resolution thermodynamic snow/ice model (HIGHTSI) is applied to simulate snow and ice thickness along the buoy drift trajectory, and we compare the model results against buoy data. We further compare the snow and ice conditions in the CHINARE region between year 2003–2004 and 2014–2015.

2 Data and model

2.1 *Buoy deployment*

During CHINARE 2003, two Zeno® ice buoys (B27823 and B27824) were deployed using a helicopter on two large multi-year ice floes, with sizes of 35 km² (B27823) and 20 km² (B27824). The ice surface was rather flat. The initial distance between B27823 and B27824 was about 200 km, and remained less than 300 km during the ice drift (Fig. 1). Both Zeno® buoys were equipped with a thermistor chain with ten sensors deployed evenly (0.32 m vertical interval) from ice surface downward. The air temperature was measured at the height of 2.5 m above the ice surface. The ocean temperature and salinity were measured at the depths of 5.6 m (B27823) and 5.9 m (B27824) below the ice surface. The buoys applied the Argos system for data transmission. The temperature and salinity measurements were taken a couple of times each day. After data quality control, the measurements were interpolated to 1 h intervals.

During CHINARE 2014, two SIMBA buoys (labelled as NMEFC02 and NMEFC03) were deployed on sea ice north of the Beaufort Gyre in the Western Arctic. The SIMBA buoys measured the vertical temperature profile of the air-snow-ice-ocean system using a high-resolution ice thermistor chain. A total of 240 sensors were mounted on the thermistor string with 2 cm intervals. The GPS position was recorded every 2 h. The temperature measurements were made 4 times a day. Additionally, each thermistor sensor was powered by two successive short heating cycles (of the order of 1–2 min) once per day. All the data were transmitted via Iridium satellite on a daily basis. The average distance between NMEFC02 and NMEFC03 was 170 km from August to November 2014.

At the time of buoy deployments during CHINARE 2003 and CHINARE 2014, sea ice was not flooded, i.e., the ice freeboard was positive (Fig. 2), and the ice surface temperature was below zero. The snow and ice thicknesses, sensor distributions and buoy operation periods are summarized in Table 1.

The Zeno® buoys worked for 5 to 8 months during 2003–2004 season, but SIMBA buoys worked much longer, for 12 to 15 months during 2014–2015 season.

2.2 *Weather data*

In order to carry out snow and ice modelling experiments, the short-term analyses and forecasts of the European Centre for Medium-Range Weather Forecasts (ECMWF) numerical weather prediction (NWP) model were used as weather forcing. Analyses with 6 h intervals were applied for the following variables: 2-m air temperature (T_a), dew-point temperature (T_d), 10-m wind speed (V_a), and total cloud cover (CN). The downward solar shortwave (Q_s) and thermal longwave (Q_l) radiative fluxes were 12-h operational forecasts, and the snow precipitation ($PrecS$) was 24-h forecast. The ECMWF products were retrieved from entire CHINARE domain (Fig. 1) with a spatial resolution of 0.125° from 1 September 2003 to 29 February 2004 for CHINARE 2003, and from 1 August 2014 to 30 September 2015 for CHINARE 2014. The T_a, T_d, V_a, CN and $PrecS$ were spatially interpolated along the

Fig. 2. The Zeno® and SIMBA (NMEFC02) deployed during CHINARE 2003 (a), and CHINARE 2014 (b); and a schematic illustration of NMEFC02 vertical sensor distribution is given (c).

Table 1. Buoy operation periods, initial deployment status and onsite snow and ice thickness

Buoy index		B27823	B27824	NMEFC02	NMEFC03
Buoy type		Zeno®	Zeno®	SIMBA	SIMBA
Observation period	starting date	2003-08-27	2003-06-9	2014-08-20	2014-08-28
	ending date	2004-05-16	2004-02-20	2015-12-02	2015-08-23*
Initial condition	snow thickness/m	0.1	0.15	0.07	0.075
	ice thickness/m	4.4	3.6	1.94	1.18
Sensor number	in the air	1	1	1–37	1–40
	in the snow	–	–	38–40	41–44
	in the ice	10	10	41–138	45–103
	in the water	1	1	139–240	104–240

Note: The sea water temperature below the ice bottom was –1.5°C for CHINARE 2003 and –1.2°C for CHINARE 2014. The ocean salinity below the ice bottom was 39.6 and 27.3, respectively. * NMEFC03 GPS stopped working in November 2014.

buoy drift trajectory and further linearly interpolated to 1 h time intervals for ice modelling.

In order to evaluate the quality of weather forcing data, we compared the observed and ECWMF-based air temperatures along the buoy drift trajectories. The synoptic and seasonal-scale temporal variability was well caught by the ECMWF air temperature analysis (not shown), but on average the ECWMF overestimated the near-surface air temperature (Table 2). The small bias of B27824 was caused by compensating periods of overestimated and underestimated of air temperature. The ECMWF air temperature had a better accuracy for CHINARE 2014 than for CHINARE 2003.

Table 2. Bias, mean absolute error (MAE), root-mean-squared error (RMSE) and correlation coefficient of ECMWF analysis air temperature compared to buoy observations

	Bias	MAE	RMSE	Corr. coefficient
B27823	1.86°C	4.3°C	5.5°C	0.91
B27824	0.09°C	4.6°C	5.9°C	0.87
NMEFC02	0.34°C	2.2°C	3.1°C	0.98
NMEFC03	0.61°C	1.7°C	2.2°C	0.95

Note: The buoy measurements were not included in the ECWMF data assimilation system. A negative/positive bias indicates an underestimation/overestimation by the model.

2.3 *Model*

A numerical model HIGHTSI (high-resolution thermodynamic snow and ice) was applied to simulate snow and ice thickness along the buoy drift trajectories. HIGHTSI is a one-dimensional snow/ice physical model targeted to solve the snow/ice surface temperature, in-snow/ice temperature and snow/ice thickness (Launiainen and Cheng, 1998). The model includes surface heat/mass balance with air-ice interactions, parameterization of snow properties and surface albedo, penetrating solar radiation in snow/ice, heat conduction equations in snow/ice, sub-surface melting, and heat/mass balance at the ice bottom.

The upper boundary conditions are given as the surface heat and mass balance equation, which yields the surface temperature and melting. A constant ocean freezing temperature is assumed, and the bottom freezing or melting is calculated from the difference between the conductive heat flux and the oceanic heat flux at the ice-ocean interface. The in-snow and in-ice temperatures are solved by partial differential heat conduction equation. The details of model physics can be found in Cheng and Launiainen (1998). The model has been applied in numerous studies on sea ice (Vihma et al., 2002; Cheng et al., 2003, 2006, 2008) and lakes ice (Semmler et al., 2012; Yang et al., 2012, 2013; Cheng et al., 2014).

The radiative fluxes in the HIGHTSI are parameterized (Launiainen and Cheng, 1998). We apply shortwave and longwave radiative fluxes parameterization schemes of Shine (1984) and Efimova (1961), respectively. The cloud effect is taken into account according to Bennett (1982) for shortwave radiation and according to Jacobs (1978) for longwave radiation. The model parameters and configurations are based on previous studies of Cheng et al. (2008) and Wang et al. (2015). In this study, the initial snow and ice thicknesses and temperatures were based on

manual measurements at the time of buoy deployment, and the model equations were integrated over the buoys' life time.

3 Results and discussion

3.1 *Estimation of snow thickness from CHINARE 2003 Zeno® buoy data*

Zeno® buoys only had air and ice temperature measurements (Fig. 3). For both B27823 and B27824, the temperature sensors were all placed in the ice floe. The initial snow thickness at the two sites differed by 5 cm from each other (Table 1). For the time period (October–February) of reliable buoy measurements, air temperatures at the buoy sites were well below the freezing point and a few degrees lower at B27823 than at B27824. The ice temperatures were, however, higher at B27823 than at B27824. Such a combination could be explained by a thicker snow pack at B2783; the strong insulation by the snow reduces the heat flux from the snow-ice interface to the snow surface, allowing surface cooling and keeping the ice relatively warm. Hence, we estimated the snow thickness for the sites of the buoys.

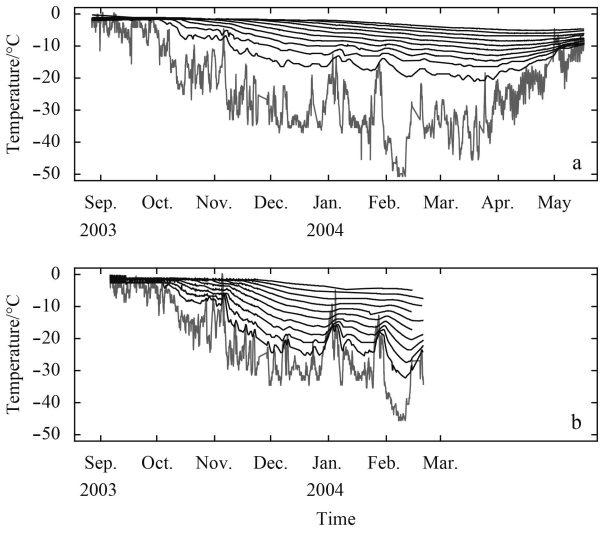

Fig. 3. The observed time series of air (grey line) and ice (black line) temperature from Zeno® buoys B27823 (a) and B27824 (b).

Considering average conditions for November–December, when the in-ice temperature was stabilized, the mean air temperatures of B27823 and B27824 were –28°C and –26°C, respectively. In winter, the surface temperature is often 2–3°C colder than the near-surface (2 m) air temperature (Persson et al., 2002). Further, we assume that the heat conductivity of snow is k_s=0.35 W/(m·K) and that of sea ice is k_i=2.1 W/(m·K). The continuity of heat flux at snow/ice interface satisfies: $-k_s\partial T/\partial z|_{snow}=-k_i\partial T/\partial z|_{ice}$. The temperatures in snow and ice are linearly distributed because it was cold and no solar radiation was available. The snow thickness at B27823 and B27824 can then be calculated using the differential equation presented above and data from the entire snow layer and the first ice layer between Sensors 1 and 2. The calculated average snow thicknesses were 23.9 cm for B27823 and 13.6 cm for B27824, which explains the warmer ice and colder air at B27823.

3.2 *Snow and ice thickness derived from SIMBA buoy data*

The retrieval of snow and ice thickness from SIMBA temperatures is largely a manual procedure currently. Based on a previous study (Cheng et al, 2015), the following assumptions are used for interface detection. (1) The temperature in air changes more rapidly than those in snow, ice and water; (2) the vertical temperature gradient in air is small; (3) the vertical temperature gradients in snow and ice differ from each other owning to their different heat conductivities; (4) the water temperature below ice floe is assumed to be constant at the freezing point, i.e., the vertical temperature gradient in the uppermost 1–2 m of the ocean is negligible; (5) the temperature raise of sensors in response to the heating cycle (2 min) was about 2°C in the air and 0.4°C in ice and 0.6°C in water, respectively (Jackson et al., 2013).

We study the vertical temperature profile through the air, snow, ice, and ocean. In cold conditions the temperature usually approximately follows a piecewise linear distribution (Leppäranta, 1993). The upper and lower ends of linear temperature profiles in snow and ice probably represent the air-snow, snow-ice and ice-water interfaces. Previous studies have indicated that the second sensor position below the cross-point of air and snow temperature profiles often represent the snow surface and it was reasonably verified by borehole measurements (Cheng et al., 2014, 2015).

A few selected NMEFC02 vertical temperature profiles are given in Fig. 4. After the deployment, temperature below the ice bottom was quite isothermal around –1.5°C. Temperatures in the thermistor chain borehole were scattered and increased close to 0°C near the ice surface and further up to 2.5°C in the air. In one week the vertical temperature adapted to a nonlinear distribution (Fig. 4, August 27). The borehole that was used to deploy the thermistor string may not necessary entirely freeze up since weather conditions in August did not favour a rapid freezing. The SIMBA temperatures suggest that a melting phase was at ice bottom from late August until mid-October. Some 20 cm ice melted at the ice bottom. Ice bottom melting from August to October was also detected previously by CRREL IMB in the CHINARE domain (Lei et al., 2014).

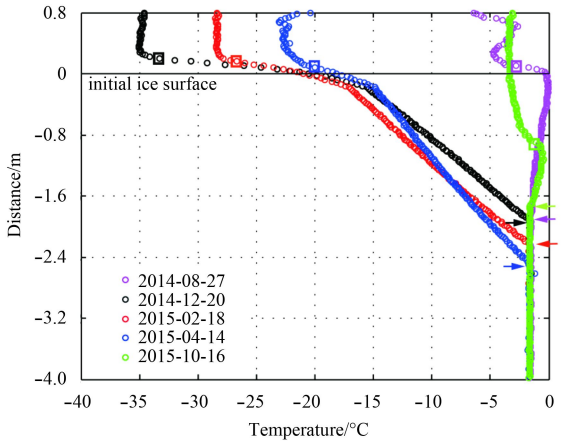

Fig. 4. Selected vertical temperature profiles measured by the NMEFC02 thermistor string at different time steps. The square marks refer to the air-snow interface and arrows the ice-ocean interface.

In cold conditions (Fig. 4, December–April), the piecewise linear vertical structure of temperatures is more clearly visible. The air-snow and ice-water interfaces are relatively easy to be detected. The snow-ice interface moves upward most likely in response to the superimposed-ice formation in summer/fall sea-

son. In winter it remained quite stable, indicating that ice thickness changes occurred mainly at the ice bottom, and snow thickness accounts upward from this reference surface. In warm conditions, the detection of the air-snow and snow-ice interfaces is more challenging. The SIMBA temperatures in late spring and summer revealed a highly nonlinear distribution in response to the solar heating and brine channel development. It is difficult to derive snow and ice thickness solely on the basis of the temperature profile. The heating cycle temperature may also be erroneous. Sometimes we need to apply a 3-point moving average calculation to improve the readability of heating temperature profiles.

The NMEFC02 temperature analyses (Fig. 5) indicated that since October 2014 the ice grew downward about 85 cm until late May 2015. By the end of November 2015, an approximately same amount of ice ablation occurred at the ice bottom. The surface melting was about 1 m and the total ice thickness was 1 m at the end of October 2015. The year-round SHEBA experiment was carried out in the CHINARE domain in 1997–1998 (Fig. 1). The ice drifted along the Beaufort Gyre northward (versus CHINARE2014 southward). During the SHEBA year, the ice bottom growth was some 65 cm from October 1997 to the end of May 1998. During summer 1998, the bottom and surface ablations were 44 cm and 75 cm, respectively. By the end of summer 1998, the total ice thickness was about 115 cm. Accordingly, ice melt both at the surface and bottom was larger during summer of 2014/2015 than the SHEBA summer. The snow and ice thickness derived from NMEFC02 temperature distribution is presented in Fig. 5 and compared with model results presented in the following section.

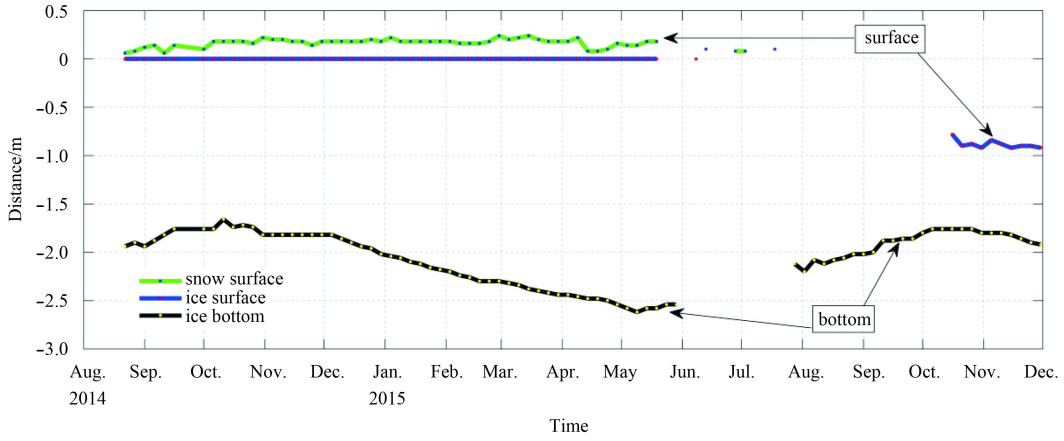

Fig. 5. Snow and ice surface, and ice bottom evolution derived from SIMBA temperature profiles. Zero distance refers to the initial snow/ice interface.

3.3 *Snow and ice modelling*

3.3.1 *CHINARE 2003*

The snow and ice thickness at Sites B27823 and B27824 were modelled and the results are shown in Fig. 6. In October 2003 snow accumulation was seen at both Sites B27823 and B27824. The difference between the two sites occurred in early November, when more snow accumulation was calculated at Site B27823. In early November, both buoys recorded a large rise of air temperature. In a cold season, the increase of air temperature

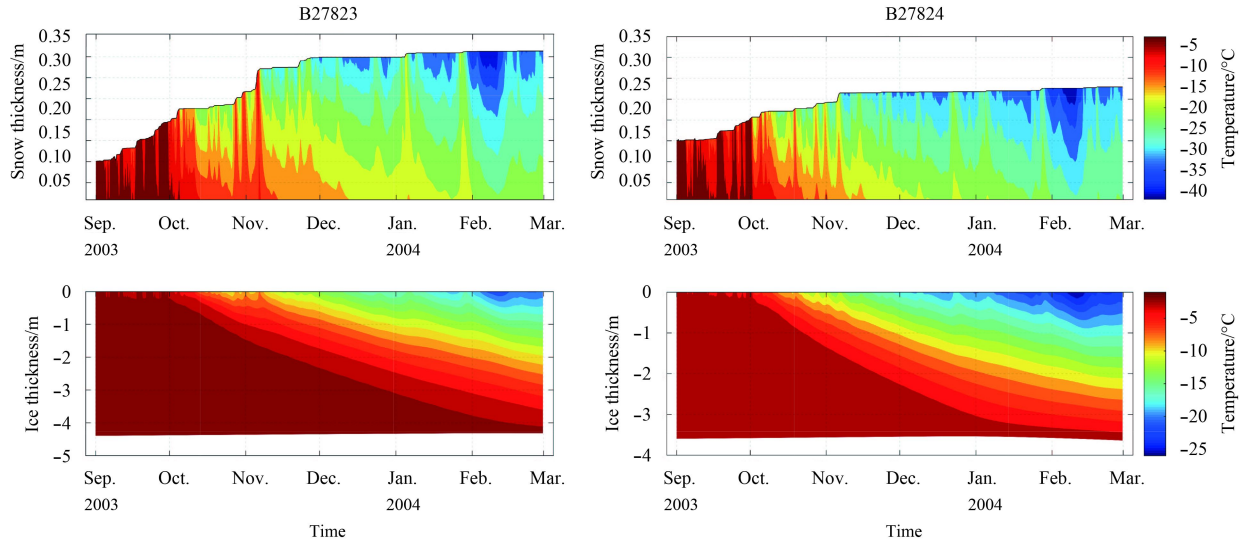

Fig. 6. HIGHTSI modelled snow and ice thicknesses as well as temperature regimes along B27823 and B27824 drift trajectories.

is often associated with a snowfall episode. The differences in modelled snow thickness at B27823 and B27834 must be due to different precipitation patterns. The different snow thicknesses were reflected in ice temperature differences, as discussed in Section 3.1.

Unfortunately, the Zeno® thermistor sting was not long enough to derive the ice thickness. We therefore only comment the modelled ice thickness. During the simulation period, ice bottom of B27823 melted roughly 10 cm before freezing started around the end of January (Day 400). For B27824, the ice bottom melted by roughly 5 cm by the end of 2003, followed by a total of 10 cm freezing until the end of March. The difference of snow thickness on top of ice later altered the temperature gradient in the ice, and eventually affected the ice mass balance at the ice bottom. At Site B27823 thicker snow reduced heat conduction upwards although the air temperature was very cold; consequently the ice bottom may encounter melting due to the constant impact of oceanic heat flux.

3.3.2 *CHINARE 2014*

The temperature measurements of both SIMBA buoys lasted long, but we only have three months of drift data from NMEFC03, since its GPS stopped working in November. Hence, we focus on modelling of NMEFC02. The snow and ice thicknesses based on NMEFC02 were compared with HIGHTSI results (Fig. 7). The observed and modelled snow thicknesses differed from each other. The NMEFC02 indicated a rather constant snow thickness in winter. A large temporal variation was detected in mid-April. The change of snow thickness was most likely due to snow drift. The modelled snow thickness showed, however, a steady snow accumulation from late August until the onset of snow melt in late May. As the effect of snow drift was not taken into account in HIGHTSI, the modelled evolution of snow thickness was mainly caused by precipitation and melt. Simple snow metamorphisms were considered in HIGHTSI (Wang et al., 2015), but those effects were of secondary importance for snow thickness. The modelled maximum snow thickness was, however, in line with the climatological snow depth in the Arctic (Warren et al., 1999; Perovich and Richter-Menge, 2015). The modelled snow-free season was from mid-June to late July. During this time ice was under a melting phase. A melting ice surface can also be confirmed by the NMEFC02 near-surface zero temperature readings during the same period.

The modelled ice thickness follows the trend yielded from NMEFC02 data analyses. The maximum modelled ice thickness was 2.6 m. At the end of simulation ice thickness was around 1.3 m.

The *in situ* measurements suggested that the ice bottom was still in a melting phase between September and October 2014. In summer, part of the solar radiation penetrates through snow, ice and melt-ponds, giving a significant contribution to increase of the oceanic heat flux. We therefore carried out an additional model experiment. Instead of a constant oceanic heat flux, we applied oceanic heat flux observed during the SHEBA experiment (Huwald et al., 2005). During SHEBA, the oceanic heat flux was 13 W/m^2 in mid-August and then reduced to 2 W/m^2 in December and gradually increased to its maximum value of 16 W/m^2 in July. Applying such a prescribed oceanic heat flux, the modelled ice thickness (black line in Fig. 7) had a better agreement with NMEFC02 ice thickness particularly in late autumn. We focus on results of this model experiment.

The modelled snow and ice temperature regimes are given in Fig. 8. The snow temperature was cold during late autumn, winter and early spring. The snow accumulation responded to the ECMWF precipitation, and snow thickness increased until

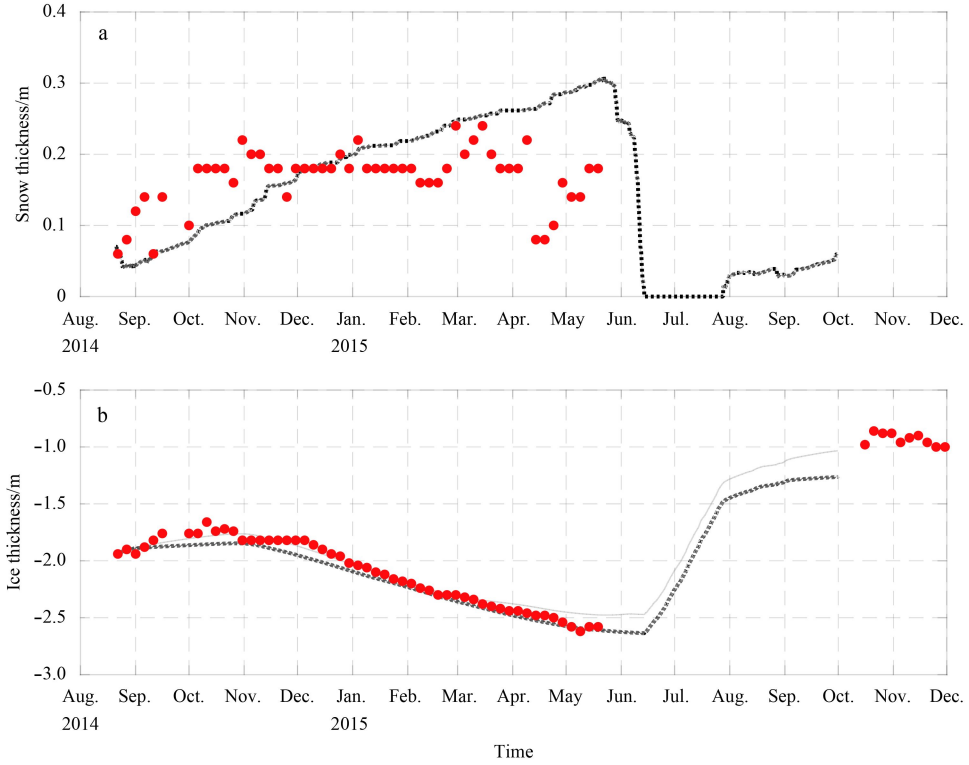

Fig. 7. HIGHTSI modelled (black line) snow and ice thickness along NMEFC02 buoy drift trajectory. The red dots are snow and ice thickness analyses based on NMEFC02 temperature measurements. The dashed line was model run using constant oceanic heat flux while the black line is model result using SHEBA observed oceanic heat flux.

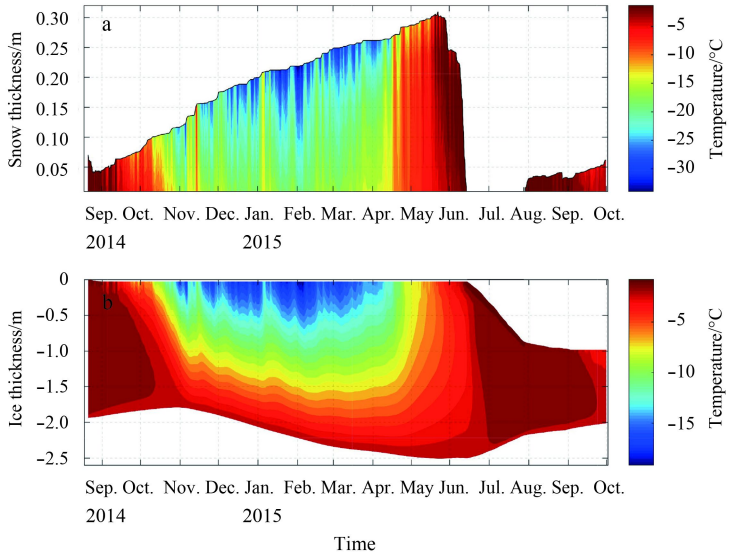

Fig. 8. Modelled snow and ice temperature regimes along NMEFC02 drift period. The moving boundaries at snow and ice surface, and ice bottom were response to the snowfall, melting and freezing, respectively.

late May, when snow-melt started. The rapid snow melt was triggered by the positive albedo feedback mechanism parameterized in the albedo scheme (Briegleb et al., 2004). The modelled ice bottom evolution was in line with NMEFC02 detection. Ice was in a freezing phase from November 2014 until May 2015 with a total freezing of 0.7 m ice at the bottom. In both 2014 and 2015, from August onwards, the ice bottom was still under a melting phase. The calculated total ice bottom melting during the whole period was about 65 cm. During the melt season, both surface and bottom melting were calculated. Surface melting dominated the total ice ablation. A total of 98 cm surface melting was calculated during snow-free season. Surface melting seems to have dominated the total ice mass balance along NMEFC02 drift trajectory, which extended far south (Fig. 1). From early June to end of July, NMEFC02 drifted to the latitude around 78.5°N. The parameterized daily mean downward solar radiation under clear skies was as high as 375 W/m^2. The large solar radiation generated significant surface and sub-surface melting calculated by HIGHTSI model. The modelled surface melt in summer was coherent with the vertical temperature profile illustrated in Fig. 4. The buoy drifted from its far north initial location south-eastward more than 500 km into the Beaufort Sea in a year and a half. The modelled ice thickness along buoy drift trajectory changed from the original 1.97 m to about 1 m.

The HIGHTSI parameterized and ECMWF forecasted daily mean downward shortwave and longwave radiative fluxes are compared in Fig. 9, demonstrating a good agreement.

The correlation coefficient between HIGHTSI and ECMWF calculated downward shortwave radiative flux was 0.95, and the value for longwave radiative flux was 0.97. The bias between HIGHTSI and ECMWF shortwave and longwave radiative fluxes were 2 W/m^2 and 7 W/m^2, respectively. The corresponding RMSE values were 27 W/m^2 and 16 W/m^2, respectively. The radiative fluxes are vital for annual sea ice surface energy balance. The agreement between the HIGHTSI and ECWMF radiative fluxes indirectly suggests that the HIGHTSI results for the surface heat balance are reasonable.

3.4 *Comparison between CHINARE 2003 and CHINARE 2014*

The average ice concentrations in August and September revealed large differences between 2003 and 2014. According to operational ice concentration products, the average ice extent and area during August and September for the entire Arctic reduced some 11% and 5% between 2003 and 2014. For the CHINARE domain, however, both the ice extent and area were larger (by 5% and 12%, respectively) in summer 2014 than in 2003. Nevertheless, the *in situ* ice thickness was evidently thinner in summer 2014 than in 2003. During both CHINARE 2003 and CHINARE 2014, it was a time consuming task to find a proper ice floe to deploy buoys, but the ice thickness differed quite a lot between the summers. During CHINARE 2003, we were still able to find a relative large flat undeformed multi-year ice floe with ice thickness of the order of 3–4 m, whereas during CHINARE 2014 the buoy could only be deployed on an ice floe less than 2 m thick. Between early August and late September, the majority of ice thicknesses measured during CHINARE 2003 were between one and two meters. During CHINARE 2014, the ice thickness survey along the ship track had a range from 0.3 m to 2.0 m, although CHINARE 2014 took place far more north than CHINARE 2003 a decade before (Fig. 1). In 2003, the ice concertation showed a large meridional gradient (Fig. 10). The heavy hummock ice located north of 80°N. R/V *Xuelong* had difficulties to sail from 80°N further north. In 2014, the ice concentration was about 100% with 10% melt pond coverage. In 2015, the ice concentration again showed a large spatial variability. NMEFC02 was located at 78.11°N, 137.21°W by the end of summer. The ice concentration was still high (about 83%) helping NMEFC02 to survive until a second winter.

The overall snow thickness in 2003 season was unusually thick in western Arctic, as also reported by other cruises. The spatial and temporal distribution of snow thickness may also be explained by the ECWMF precipitation forecasts. The annual total accumulated precipitation in the CHINARE domain during 2003–2004 and 2014–2015 are compared in Fig. 11. During 2003–2004 the high Arctic had more precipitation than the lower latitude region. The spatial distribution of total precipitation consisted with the snow depth estimation at B27823 and B27824 sites. During 2014–2015, more spatial variability was seen in annual precipitation.

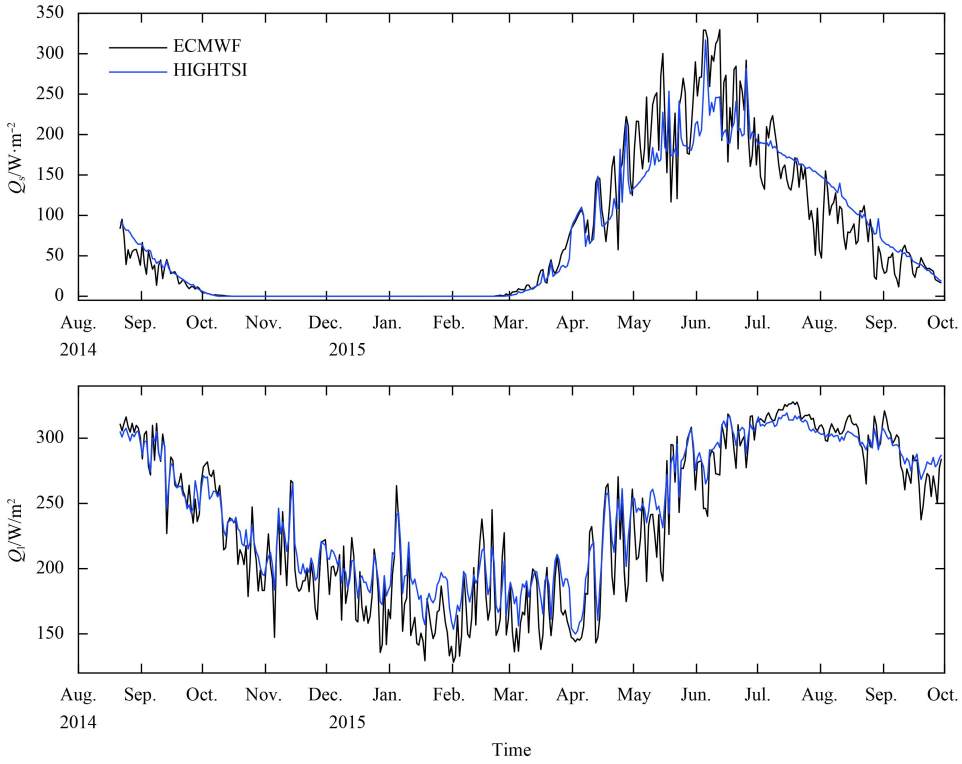

Fig. 9. HIGHTSI parameterized and ECMWF forecasted daily mean downward shortwave and longwave radiative fluxes along NMEFC02 drift trajectory.

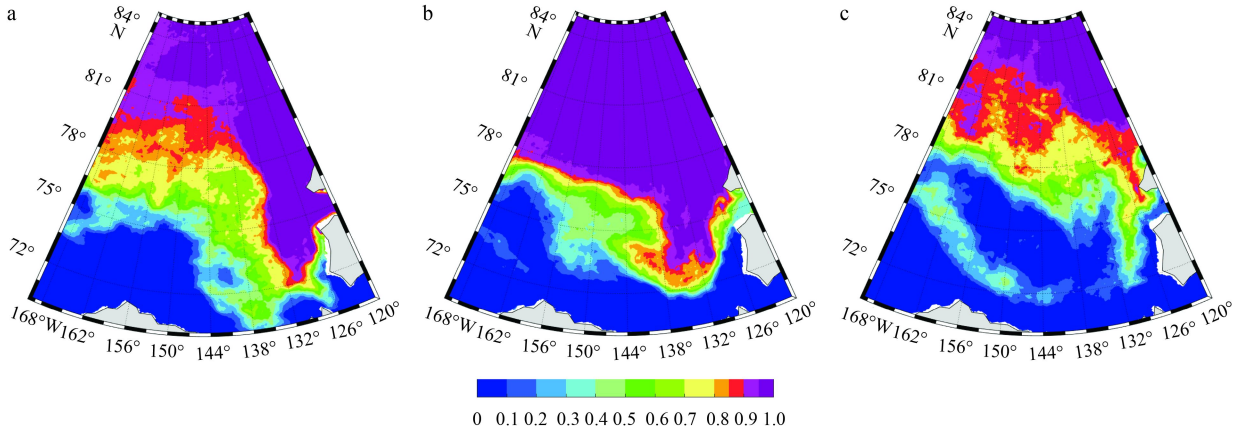

Fig. 10. Average daily ice concentration bewteen 1 August and 30 September in 2003 (a), 2014 (b) and 2015 (c). The spatial resolution is 6.25 km^2. The 2003 ice conecntration was calculated on the basis of AMSRE whereas the 2014 and 2015 ice ceoncetrations were calculated using AMSR2. The product was made by the University of Bremen.

4 Conclusions

Zeno® ice buoys and SIMBA ice mass balance buoys were deployed during CHINARE 2003 and CHINARE 2014. We applied the buoy data to investigate snow and ice thickness in the Western Arctic Ocean. A thermodynamic snow/ice model was applied to simulate snow and ice thickness along the buoy drift trajectories. Ice mass-balance buoys have been deployed in the Arctic Ocean during several CHINARE Arctic expeditions, and IMB data have been used to analyze ice thickness (Lei et al., 2014). In this study, for the first time, we presented snow and ice thicknesses derived from Zeno® and SIMBA data, and compared the results with the output of a physically based snow and ice model. We are not aware of such a study carried out before.

In cold conditions, sea ice thickness can be estimated on the basis of SIMBA high-resolution temperature profiles. The SIMBA-based ice thickness was in good agreement with model calculations. The model results can be improved by applying a prescribed oceanic heat flux based on local measurements. SIMBA measurements revealed a drift from the northern Beaufort Gyre region south-eastwards to the central Beaufort Sea in 15 months, during which the ice thickness varied from 1.97 to 2.5 m and further down to about 1 m before the buoy was lost. The model experiments revealed that the total ice mass balance was contributed by 70 cm and 65 cm of bottom freezing and melting, respectively, in 15 months, and by 98 cm of surface melting during summer 2015. A previous study has indicated that

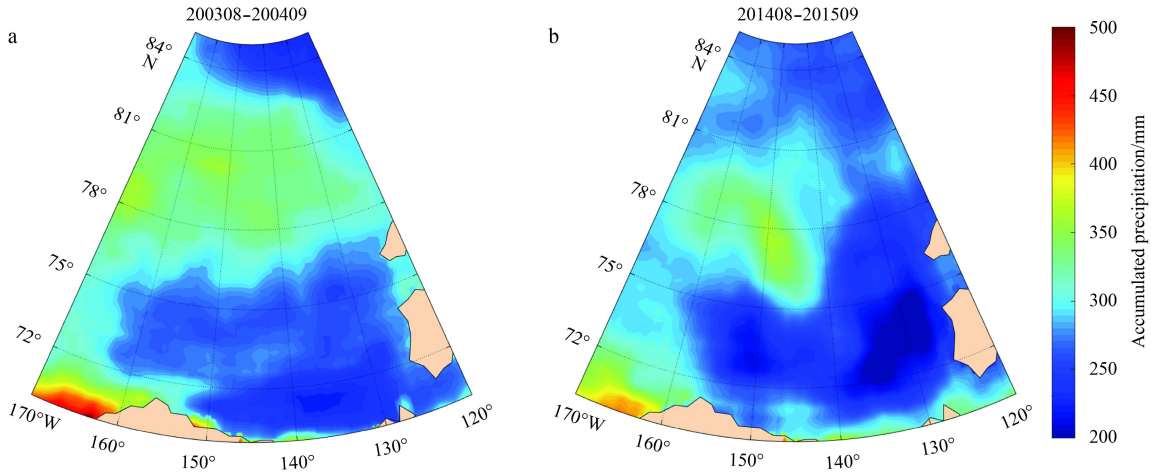

Fig. 11. The ECWMF accumulated precipitation in the CHINARE domain during 2003–2004 and 2014–2015 season.

there is a large regional and inter-annual variability of sea ice melt in the Beaufort Sea (Perovich and Richter-Menge, 2015). Our result suggested that during 2014–2015 surface melting dominated the total ice mass balance.

The ECMWF operational analyses of 2 m air temperature agreed well with buoy measurements. The accuracy of ECMWF analyses has been improved in time. The daily mean ECMWF forecasted shortwave and longwave radiative fluxes were in good agreement HIGHTSI parameterized results. Modelling of snow thickness in the Arctic Ocean is challenging, in particular the increase of snow thickness. Large uncertainty comes from the precipitation forcing. A previous study indicated that the ECMWF provides good precipitation products at high latitudes (Jakobson and Vihma, 2010). For CHINARE 2003, the modelled snow thickness at Argos buoy sites was consistent with the simple quantitative analyses using buoy ice temperature data. The regional annual total precipitation also supports buoy data analyses. For CHINARE 2014, the modelled maximum snow thickness was in line with Arctic climatological snow depth analyses (Warren et al., 1999) and buoy measurements (Perovich and Richter-Menge, 2015). HIGHTSI modelled snow-melt onset as well as snow-free time period were also consistent with the average climate conditions (Maksimovich and Vihma, 2012).

The snow thicknesses derived from buoy data and ice model differed from each other. Challenges remain in detection of the air/snow interface. The uncertainties of SIMBA air/snow interface most likely originate from the effects of snow drift, frosts on thermistor sensors, and solar heating of the sensors. Especially during summer, the substantial surface melting could alter the orientation of the thermistor string in the air, making it difficult to detect the snow/ice interface. This problem remains to be solved. In the Arctic from mid-autumn to early-spring we can assume that the snow/ice interface remains unchanged. This is because there is no more surface melt and snow accumulation is usually not enough to cause ocean flooding. This is in contrast to the situation in boreal lakes, where the snow/ice interface is a moving surface (Cheng et al., 2014). A fixed snow/ice interface makes SIMBA data adequate to retrieve ice thickness, since the ice bottom evolution is relatively easy to be detected from SIMBA temperature profiles. During early ice-melt season, however, the snow/ice interface can be affected by snow-to-ice transformation (melting snow refreezes to form superimposed ice, so the snow/ice interface moves upwards).

Currently the SIMBA temperature analyses are largely done manually. One has to look at each SIMBA temperature profile to identify the air-snow, snow-ice, and ice-ocean interfaces. If there are uncertainties, one has to look at the signal of sensor heating and apply the information empirically to help detect interfaces. A reliable algorithm is still missing in order to identify snow and ice thickness automatically. More work on SIMBA data analyses is still needed. First of all, the SIMBA snow and ice thickness should be compared with advanced ice mass balance buoy measurements (e.g., Perovich et al., 2003; Lei et al., 2014; Perovich and Richter-Menge, 2015) in order to improve the reliability of SIMBA data interpretation.

Acknowledgements

The ECMWF is acknowledged for data supply. The authors are grateful to the colleagues who have provide technical supports in the CHINARE 2003 and CHINARE 2014 field expeditions, particularly Pekka Kosloff from FMI in CHINARE 2003 and Lei Ruibo from Polar Research Institute of China (PRIC) in CHINARE 2014.

References

Bennett T J. 1982. A coupled atmosphere-sea ice model study of the role of sea ice in climatic predictability. J Atmos Sci, 39(7): 1456–1465

Blunden J, Arndt D S. 2012. State of the climate in 2011. Bull Am Meteor Soc, 93(7): S1–S282

Briegleb B P, Bitz C M, Hunke E C, et al. 2004. Scientific description of the sea ice component in the community climate system model, version three. NCAR/TN-463+STR, NCAR Tech Note. Boulder, Colorado: National Center for Atmospheric Research, 1–78

Cavalieri D J, Parkinson C L. 2012. Arctic sea ice variability and trends, 1979–2010. Cryosphere, 6(4): 881–889

Cheng Bin, Launiainen J. 1998. A one-dimensional thermodynamic air-ice-water model: technical and algorithm description report. Rep Ser Finn Inst Mar Res, 37: 15–35

Cheng Bin, Launiainen J, Vihma T. 2003. Modelling of superimposed ice formation and sub-surface melting in the Baltic Sea. Geophysica, 39(1–2): 31–50

Cheng Bin, Vihma T, Pirazzini R, et al. 2006. Modelling of superimposed ice formation during the spring snowmelt period in the Baltic Sea. Ann Glaciol, 44(1): 139–146

Cheng Bin, Vihma T, Rontu L, et al. 2014. Evolution of snow and ice temperature, thickness and energy balance in Lake Orajarvi, northern Finland. Tellus A, 66(1): 21564

Cheng Bin, Zhang Zhanhai, Vihma T, et al. 2008. Model experiments on snow and ice thermodynamics in the Arctic Ocean with CHINARE 2003 data. J Geophys Res, 113(C9): C09020

Cheng Bin, Zhao Jiechen, Vihma T. 2015. Detection of snow and ice thickness from temperature profiles of unmanned ice mass balance buoys. In: Proceedings of the 30th International Symposium on Okhotsk Sea and Sea Ice. Mombetsu, Hokkaido, Japan: Okhotsk Sea and Cold Ocean Research Association

Efimova N A. 1961. On methods of calculating monthly values of net longwave radiation. Meteor Gidrol, 10: 28–33

Gascard J C, Festy J, le Goff H, et al. 2008. Exploring Arctic transpolar drift during dramatic sea ice retreat. EOS, 89(3): 21–22

Huwald H, Tremblay L B, Blatter H. 2005. Reconciling different observational data sets from surface heat budget of the Arctic Ocean (SHEBA) for model validation purposes. J Geophys Res, 110(C5): C05009

Jackson K, Meldrum D, Wilkinson J, et al. 2013. A novel and low cost sea ice mass balance buoy. Journal of Atmospheric & Oceanic Technology, 30(11): 2676–2688

Jacobs J D. 1978. Radiation climate of Broughton Island. In: Barry R G, Jacobs J D, eds. Energy Budget Studies in Relation to Fast-Ice Breakup Processes in Davis Strait. Occasional Paper 26. Boulder, USA: Inst Arctic Alpinc Res, Univ of Colorado, 105–120

Jakobson E, Vihma T. 2010. Atmospheric moisture budget in the Arctic based on the ERA-40 reanalysis. Int J Climatol, 30(14): 2175–2194

Kwok R, Rothrock D A. 2009. Decline in Arctic sea ice thickness from submarine and ICESat records: 1958–2008. Geophys Res Lett, 36(15): L15501

Launiainen J, Cheng Bin. 1998. Modelling of ice thermodynamics in natural water bodies. Cold Reg Sci Technol, 27(3): 153–178

Lei Ruibo, Li Na, Heil P, et al. 2014. Multiyear sea ice thermal regimes and oceanic heat flux derived from an ice mass balance buoy in the Arctic Ocean. J Geophys Res, 119(1): 537–547

Leppäranta M. 1993. A review of analytical models of sea-ice growth. Atmosphere-Ocean, 31(1): 123–138

Maksimovich E, Vihma T. 2012. The effect of surface heat fluxes on interannual variability in the spring onset of snow melt in the central Arctic Ocean. J Geophys Res, 117(C7): C07012

Perovich D K, Grenfell T C, Richter-Menge J A, et al. 2003. Thin and thinner: sea ice mass balance measurements during SHEBA. J Geophys Res, 108(C3): 8050

Perovich D K, Richter-Menge J A. 2015. Regional variability in sea ice melt in a changing Arctic. Philos Trans Royal Soc A Math Phys Eng Sci, 373(2045): 20140165

Persson P O G, Fairall C W, Andreas E L, et al. 2002. Measurements near the Atmospheric Surface Flux Group tower at SHEBA: near-surface conditions and surface energy budget. J Geophys Res Atmos, 107(C10): 8045

Richter-Menge J A, Perovich D K, Elder B C, et al. 2006. Ice mass-balance buoys: a tool for measuring and attributing changes in the thickness of the Arctic sea-ice cover. Ann Glaciol, 44(1): 205–210

Semmler T, Cheng Bin, Yang Yu, et al. 2012. Snow and ice on Bear Lake (Alaska) - sensitivity experiments with two lake ice models. Tellus A, 64(1): 17339

Shine K P. 1984. Parametrization of the shortwave flux over high albedo surfaces as a function of cloud thickness and surface albedo. Quart J Roy Meteor Soc, 110(465): 747–764

Uttal T, Curry J A, Mcphee M G, et al. 2002. Surface heat budget of the Arctic Ocean. Bull Am Meteor Soc, 83(2): 255–276

Vihma T, Uotila J, Cheng Bin, et al. 2002. Surface heat budget over the Weddell Sea: buoy results and model comparisons. J Geophys Res, 107(C2): 3013

Wang Caixin, Cheng Bin, Wang Keguang, et al. 2015. Modelling snow ice and superimposed ice on landfast sea ice in Kongsfjorden, Svalbard. Polar Res, 34(1): 20828

Warren S G, Rigor I G, Untersteiner N, et al. 1999. Snow depth on Arctic sea ice. J Climate, 12(6): 1814–1829

Yang Yu, Cheng Bin, Kourzeneva E, et al. 2013. Modelling experiments on air-snow-ice interactions over Kilpisjärvi, a lake in northern Finland. Boreal Environ Res, 18(5): 341–358

Yang Yu, Leppäranta M, Cheng Bin, et al. 2012. Numerical modelling of snow and ice thicknesses in Lake Vanajavesi, Finland. Tellus A, 64(1): 17202

Zhang Zhanhai. 2004. The Report of 2003 Chinese Arctic Research Expedition (in Chinese). Beijing: China Ocean Press, 1–229